energies

MDPI

Article

Effect of Draft Tube Vortex Rope on Shaft System Mechanical Response in Pump-Turbines

Yanhao Li [1], Likun Ding [2], Lei Chen [2] and An Yu [2,*]

[1] Shanghai Investigation, Design & Research Institute Co., Ltd., Shanghai 200335, China; li_yanhao@ctg.com.cn
[2] School of Electrical and Power Engineering, Hohai University, Nanjing 211100, China; dlk2294269757@163.com (L.D.); chenlei202310@163.com (L.C.)
* Correspondence: yu_an@hhu.edu.cn; Tel.: +86-15190490883

Abstract

During frequent peak-regulation operation, pumped storage units inevitably operate under off-design conditions. Variations in draft tube flow structures under different load conditions may alter the hydraulic loading acting on the runner and shaft system. In this study, a model pump-turbine was investigated using unsteady numerical simulations combined with finite element structural analysis. Analyses were conducted under 70%, 100%, and 105% load conditions, representing typical part-load, rated, and overload operating states. The results show that under 70% load, the draft tube flow exhibits an eccentric structure with strong circumferential pressure non-uniformity. At the rated condition (100% load), the flow field is closest to axisymmetric with the most uniform pressure distribution. Under 105% load, a concentrated central vortex forms, and the degree of non-uniformity is intermediate. The hydraulic loads under different conditions lead to significant differences in the stress and deformation characteristics of the shaft system. The maximum equivalent stress increases from 1.84 MPa at the rated condition to 3.33 MPa under overload conditions, while more pronounced flow asymmetry and pressure non-uniformity occur at part-load operation. These findings clarify the relationship between load variation, draft tube flow structures, and the mechanical response of the shaft system.

Keywords: pump-turbine; draft tube vortex rope; shaft system response; fluid–structure interaction; stress analysis

1. Introduction

With the continuous increase in installed renewable energy capacity, power systems have imposed higher demands on peak shaving and frequency regulation. Pumped storage units, therefore, play an increasingly important role in grid stabilization. As the core component of pumped storage stations, pump-turbines frequently switch between generating and pumping modes during operation. Consequently, operation under various off-design conditions becomes unavoidable, and the running time at partial load and low discharge conditions is significantly increased.

Under such conditions, a rotating vortex rope is likely to develop in the draft tube, accompanied by pronounced low-frequency pressure pulsations. These pressure fluctuations can be transmitted to the runner and main shaft system through hydraulic excitation, leading to unit mechanical response and, in severe cases, resonance and structural damage. Therefore, it is necessary to systematically investigate the formation characteristics of draft tube vortex ropes and their influence on unit mechanical response.

Check for updates

Academic Editor: Mahmoud Bourouis

Received: 2 March 2026
Revised: 29 March 2026
Accepted: 31 March 2026
Published: 7 April 2026

Copyright: © 2026 by the authors. Licensee MDPI, Basel, Switzerland. This article is an open access article distributed under the terms and conditions of the Creative Commons Attribution (CC BY) license.

Extensive research has been conducted on the operation and stability of pumped storage systems under varying load conditions. As key components of such systems, pump-turbines frequently operate away from the design point during peak regulation, where complex internal flow phenomena may significantly affect unit performance and safety.

In conventional hydraulic machinery, considerable attention has been paid to draft tube vortex ropes and the associated pressure pulsation phenomena. Ruprecht et al. [1] carried out numerical simulations to investigate the formation of vortex ropes and their pressure pulsation characteristics under part-load conditions, with good agreement between numerical and experimental results. Kirschner et al. [2] conducted experimental studies on the relationship between vortex rope motion and pressure pulsations, showing that both low- and high-frequency fluctuations are closely related to vortex rotation. Muntean et al. [3] used combined experimental and numerical approaches to analyze the unsteady pressure field induced by precessing vortex ropes, indicating that low-frequency synchronous pulsations are a major source of instability. Skripkin et al. [4] employed high-speed visualization to investigate vortex rope separation and vortex ring formation, revealing strong pressure impacts along the draft tube wall. Cheng et al. [5] analyzed the characteristics of helical vortex ropes and proposed an engineering method for evaluating vortex rope intensity.

With the advancement of research, increasing attention has been given to the formation mechanisms and evolution processes of vortex ropes. Favrel et al. [6] showed that the precession frequency of vortex ropes can be characterized by the outlet swirl number and proposed a method for predicting resonance conditions. Sotoudeh et al. [7] investigated vortex rope formation during load variation and identified its evolution stages. Jin et al. [8] applied large eddy simulation to analyze the spatiotemporal evolution of vortex ropes, while Li et al. [9] used entropy production theory and chaos analysis to reveal energy distribution and pressure pulsation characteristics. Susan-Resiga et al. [10] proposed a jet control method to suppress vortex rope development, and Shtork et al. [11] reviewed various control techniques, including air admission and jet injection, for reducing pressure pulsations.

For pump-turbines, both experimental and numerical studies have been carried out on draft tube vortex rope characteristics. Lai et al. [12] used LDV measurements to obtain velocity distributions and capture vortex rope structures and their precession frequencies. Kim et al. [13] investigated the interaction between blade passage vortices and draft tube vortex ropes, showing that their combined effect leads to significant pressure pulsations under low-discharge conditions. He et al. [14] reported that vortex structures become more pronounced at low flow rates and may induce unit vibration. Xin et al. [15] studied the interaction between vortex ropes and cavitation, while Pang et al. [16] analyzed the influence of cavitation intensity on vortex rope morphology and dominant frequencies. Liu et al. [17] applied POD and DMD methods to identify dominant vortex structures and their influence on flow energy distribution.

Under off-design and transient operating conditions, vortex rope behavior becomes more complex. Mao et al. [18] analyzed vortex evolution during load rejection, while Zhang et al. [19] showed that pressure pulsations under S-shaped operating conditions result from the combined effects of rotating stall and vortex ropes. Li et al. [20] demonstrated that guide vane optimization can effectively reduce vortex rope intensity and pressure pulsations. These studies have significantly improved the understanding of flow instability, but are mainly focused on flow behavior itself.

In addition to flow studies, the influence of hydraulic phenomena on structural response has also attracted attention. Trivedi et al. [21] reviewed fluid–structure interaction issues in hydraulic machinery and pointed out that pressure pulsations may lead to fa-

tigue failure and resonance risks. Wang et al. [22] and Anup et al. [23] investigated the effects of rotor–stator interaction and vortex ropes on pressure and torque fluctuations. Xia et al. [24] analyzed the modal characteristics of runners using the finite element method and highlighted the potential for modal coupling between the runner and shafting system.

Research on shaft systems has mainly focused on dynamic characteristics and multi-field coupling effects. Xu et al. [25,26] studied nonlinear dynamics and modal coupling of hydro-generator units. Niu et al. [27] investigated the effects of shaft eccentricity and bearing stiffness on vibration characteristics. Ma et al. [28] established a hydro-mechanical-electrical coupled model to analyze nonlinear behavior during start-up conditions. Cao et al. [29] reviewed the development of multi-field coupling in turbine rotor systems. However, most existing studies treat flow and structural responses separately, and systematic investigations into the relationship between draft tube vortex rope characteristics and shaft system mechanical response remain limited.

In summary, existing studies have systematically clarified the formation mechanisms, evolution characteristics, and pressure pulsation behavior of draft tube vortex ropes, and have also investigated shaft system response to a certain extent. However, most previous work has focused separately on either flow instability or structural analysis. Systematic investigations into the relationship between vortex rope-induced hydraulic loads and shaft structural response remain limited, particularly under the typical partial-load conditions of pump-turbines, where the underlying mechanisms have yet to be fully elucidated.

Therefore, this study aims to quantitatively investigate the influence of draft tube vortex rope characteristics on the mechanical response of the shaft system in a pump-turbine. The research is conducted in four stages. First, a three-dimensional unsteady CFD model is established to simulate the transient flow field under different load conditions. Second, the evolution of vortex rope structures and the associated pressure pulsation characteristics are analyzed to identify dominant frequencies and flow features. Third, the transient pressure fields are extracted and mapped as equivalent hydraulic loads onto the runner surfaces. Finally, a finite element model of the shaft system is employed to evaluate the resulting stress and deformation.

Based on these analyses, the study establishes a quantitative link between flow instability, hydraulic load variation, and structural response, providing insight into the mechanical behavior of pump-turbines under off-design operating conditions.

2. Materials and Methods

2.1. Mathematical Model

2.1.1. Governing Equations

The internal flow of the pump-turbine mainly uses water as the working medium, and the heat transfer process is usually neglected. Therefore, the energy equation is not considered in the calculations. The fluid is treated as an incompressible medium with constant density. Based on the above assumptions, the governing equations include the mass conservation equation (continuity equation) and the momentum conservation equation (Navier–Stokes equations, N–S equations). The governing equations are given as follows:

$$\frac{\partial \rho}{\partial t} + \frac{\partial (\rho u)}{\partial x} + \frac{\partial (\rho v)}{\partial y} + \frac{\partial (\rho w)}{\partial z} = 0 \tag{1}$$

$$\frac{\partial (\rho U_i)}{\partial t} + \frac{\partial (\rho U_i U_j)}{\partial x_j} = -\frac{\partial P}{\partial x_i} + \frac{\partial}{\partial x_j}\left[(\mu + \mu_{tur}) \left(\frac{\partial U_i}{\partial x_j} + \frac{\partial U_j}{\partial x_i} - \frac{2}{3}\frac{\partial U_k}{\partial x_k}\delta_{ij} \right) \right] \tag{2}$$

where ρ, U, P, and t represent the fluid density, time-averaged velocity, pressure, and time, respectively. μ and μ_{tur} denote the dynamic viscosity and turbulent viscosity, respectively.

2.1.2. Turbulence Model

To balance computational efficiency and accurate capture of draft tube vortex structures under multiple operating conditions, the SST k–ω turbulence model was adopted for numerical simulation. Compared with other turbulence models, the large eddy simulation (LES) method can effectively resolve small-scale vortex structures but requires excessive computational resources, making it unsuitable for multi-condition parametric studies. The standard k–ε model has relatively high computational efficiency but relies on wall functions to treat near-wall flows, resulting in limited accuracy under strong adverse pressure gradients and flow separation conditions. Although the standard k–ω model provides better prediction accuracy in the near-wall region, it requires relatively higher computational cost for overall flow field simulation. The SST k–ω model combines the advantages of the k–ε and k–ω models [30]. By introducing a shear stress transport mechanism into the turbulent viscosity formulation, the SST k–ω model improves the prediction accuracy for flows with strong adverse pressure gradients and flow separation. Therefore, compared with the standard k–ω model, the SST k–ω model provides higher numerical accuracy in simulating complex vortex flows such as draft tube swirling flows. The transport equations for turbulent kinetic energy k and specific dissipation rate ω are given as follows [31,32]:

$$\frac{\partial k}{\partial t} + \overline{u_j}\frac{\partial k}{\partial x_j} = P_k + \frac{\partial}{\partial x_j}\left[(\nu + \sigma_k \nu_t)\frac{\partial k}{\partial x_j}\right] - \beta^* k\omega \tag{3}$$

$$\frac{\partial \omega}{\partial t} + \overline{u_j}\frac{\partial \omega}{\partial x_j} = \alpha S^2 - \beta\omega^2 + \frac{\partial}{\partial x_j}\left[(\nu + \sigma_{\omega 1}\nu_t)\frac{\partial \omega}{\partial x_j}\right] + 2(1 - F_1)\sigma_{\omega 2}\frac{1}{\omega}\frac{\partial k}{\partial x_i}\frac{\partial \omega}{\partial x_i} \tag{4}$$

where the expression of F_1 is given as follows:

$$F_1 = \tanh\left\{\left\{\min\left[\max\left(\frac{\sqrt{k}}{\beta^*\omega y}, \frac{500\nu}{y^2\omega}\right), \frac{4\sigma_{\omega 2}k}{CD_{k\omega}y^2}\right]\right\}^4\right\} \tag{5}$$

$$CD_{k\omega} = \max\left(2\rho\sigma_{\omega 2}\frac{1}{\omega}\frac{\partial k}{\partial x_i}\frac{\partial \omega}{\partial x_i}, 10^{-10}\right) \tag{6}$$

The turbulent viscosity is defined as:

$$\nu_t = \frac{\alpha_1 k}{\max(\alpha_1\omega, SF_1)} \tag{7}$$

F_1 is a blending function representing the weighting of the two turbulence models in the computational domain. Y denotes the distance from the wall. β^*, $\sigma_{\omega 1}$, $\sigma_{\omega 2}$ are empirical constants determined from experimental measurements. Here, β^* = 0.09, $\sigma_{\omega 1}$ = 0.5, $\sigma_{\omega 2}$ = 0.856.

In the structural analysis, the equivalent hydraulic loads extracted under different operating conditions were applied to the finite element model of the shaft system to perform equivalent structural calculations, thereby obtaining the equivalent stress distribution of the shaft system and the overall deformation characteristics of the runner. The material properties, boundary conditions, and connection relationships of the shaft system model were established according to the actual unit configuration. By comparing the stress levels and deformation modes of the shaft system under different load conditions, the influence of draft tube flow structure variations on the equivalent mechanical state of the shaft system can be systematically evaluated. This approach establishes a direct correspondence between flow structures and the mechanical response of the shaft system within an unsteady com-

putational framework, providing a basis for structural safety assessment under different operating conditions.

2.1.3. Fluid–Structure Interaction (FSI) Theory

A one-way fluid–structure interaction (FSI) approach was adopted. At the coupling interface, the flow field simulation results were transferred to the solid domain for structural analysis. Within this domain, physical quantities such as displacement and stress at the fluid–structure interface were required to satisfy compatibility and equilibrium conditions. The governing equations are expressed as follows:

$$\tau_f n_f = \tau_s n_s \tag{8}$$

$$d_f = d_s \tag{9}$$

where $\tau_f n_f$ and $\tau_s n_s$ denote the normal stresses of the fluid and solid at the coupling interface, respectively; d_f and d_s represent the fluid and solid displacements at the interface.

2.2. Numerical Set Up and Validation

2.2.1. Computational Model of the Fluid Domain

The research object of this study is a model pump-turbine. The computational domain includes the spiral casing, stay vanes, guide vanes, runner, and draft tube. The computational mesh of the fluid domain was generated using structured hexahedral elements to ensure numerical accuracy and convergence stability. The model and mesh of the pump-turbine are shown in Figures 1 and 2, respectively. The main parameters of the unit are listed in Table 1.

Table 1. Basic parameters of pump turbine.

Parameter	Value
Runner inlet diameter D2	0.442 m
Runner outlet diameter D1	0.3 m
Number of runner blades	9
Number of stay vanes	20
Number of guide vanes	20
Rate rotation speed	1500 r/min
Draft tube height	1.1092 m
Draft tube length	2.4723 m

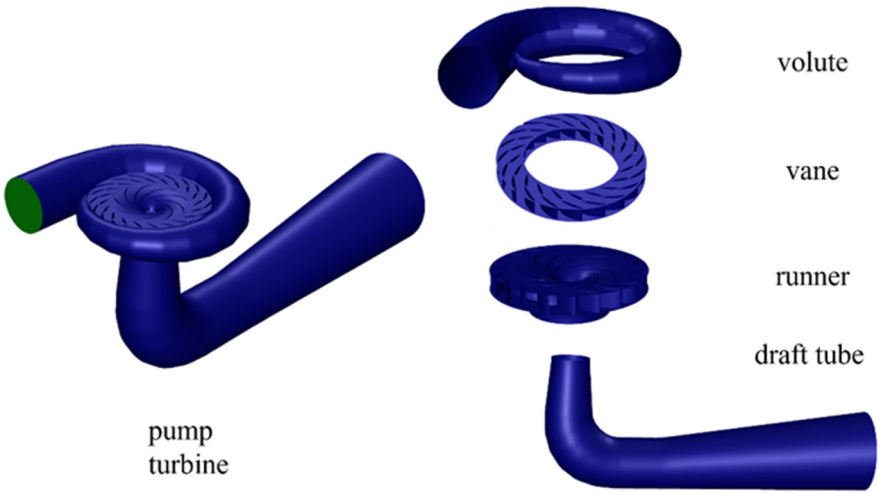

Figure 1. Physical model of pump turbine [33].

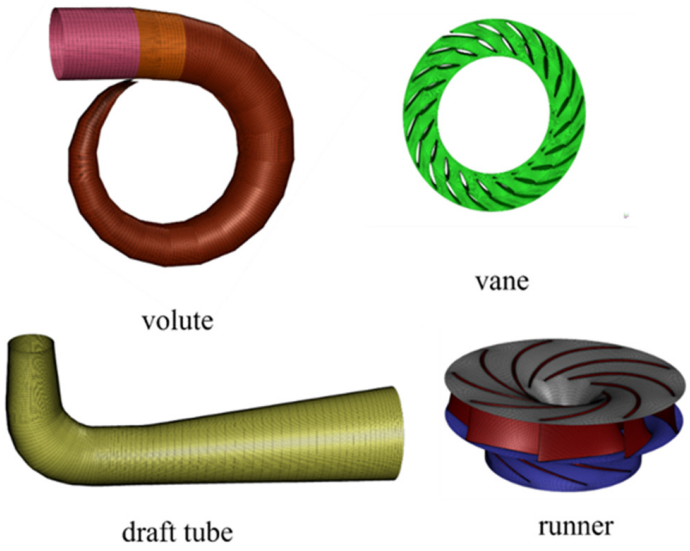

Figure 2. Computational domain mesh.

2.2.2. Structural Model of the Shaft System

The structural material of the pumped storage unit is structural steel. The structural model was meshed using unstructured tetrahedral elements in ANSYS Workbench 2022 R1, and local mesh refinement was applied to the runner region to improve the accuracy of the numerical results in critical areas. The final mesh of the unit foundation structure consisted of approximately one million elements, with local refinement in the runner region. First, unsteady flow field simulations were performed in ANSYS Fluent 2022 R1 to obtain the instantaneous pressure field at several typical moments under different load conditions. The runner blade surfaces were then defined as hydraulic pressure boundaries, and the corresponding instantaneous pressure data were mapped onto the structural model. Subsequently, static equivalent structural analyses were conducted in ANSYS Mechanical 2022 R1. The water guide bearing, upper guide bearing, and lower guide bearing were used to constrain radial mechanical response, while the thrust bearing was applied to restrict axial mechanical response. In this study, these bearing positions were modeled using elastic supports to calculate the shaft displacement at the corresponding locations. Through this procedure, the transient flow field pressure was equivalently transferred to the shaft system structural model, providing a basis for analyzing the stress distribution of the shaft system and the deformation characteristics of the runner under different operating conditions. In the present study, a one-way fluid–structure interaction (FSI) approach was adopted. The unsteady pressure field obtained from CFD simulations was mapped onto the structural model for subsequent analysis. After the flow field reached a statistically stable state, pressure data from one complete runner revolution were selected. Four representative time instants within one rotational period (T_0–T_3) were extracted to characterize the temporal variation in hydraulic loading. The pressure loads were applied to the wetted surfaces of the runner blades as surface pressure distributions, rather than the full flow field. The data transfer between the fluid and structural domains was performed through pressure mapping from ANSYS Fluent to ANSYS Mechanical. Based on these mapped pressure loads, static structural analyses were conducted to evaluate the stress and deformation characteristics of the shaft system. The relevant structural parameters of the unit are listed in Table 2, and the mesh distribution and constraint conditions of the shaft system model are shown in Figure 3.

Table 2. Pump turbine structure parameter setting.

Project	Value	Unit
Density	7850	kg/m^3
Young's Modulus	200	GPa
Poisson's Ratio	0.3	
Gravitational Acceleration	9.8066	m/s^2
Rated Rotational Speed	1500	r/min
Stiffness Coefficient of the Upper Guide Bearing	8×10^9	N/m^3
Stiffness Coefficient of the Lower Guide Bearing	8×10^9	N/m^3
Stiffness Coefficient of the Water Guide Bearing	5×10^9	N/m^3

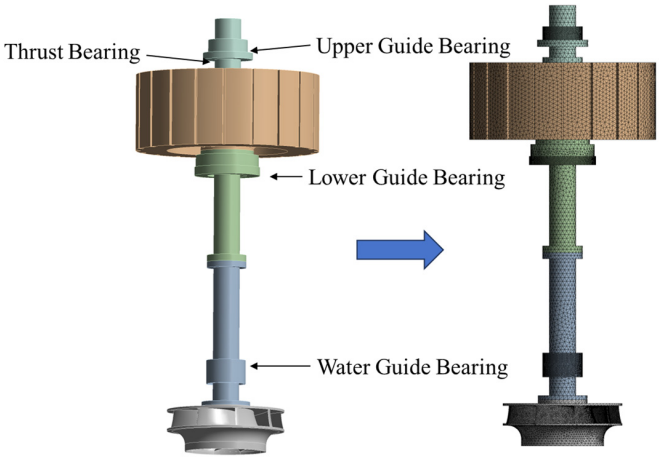

Figure 3. Tetrahedral mesh and constraint conditions of pump turbine shafting.

The computational mesh of the fluid domain was generated using structured hexahedral elements, while the structural model of the shaft system was meshed using unstructured tetrahedral elements. A numerical simulation of the pump-turbine under the design operating condition was conducted to verify grid independence, and the results are presented in Figure 4. As shown in Figure 4, when the total number of grid elements exceeded 3.15 million, the flow rate converged to approximately 634 L/s, with a deviation of less than 5% compared to the experimental value. Therefore, this mesh density satisfies the accuracy requirements while effectively reducing computational cost. Finally, a total of 3.15 million grid elements was adopted for the subsequent simulations.

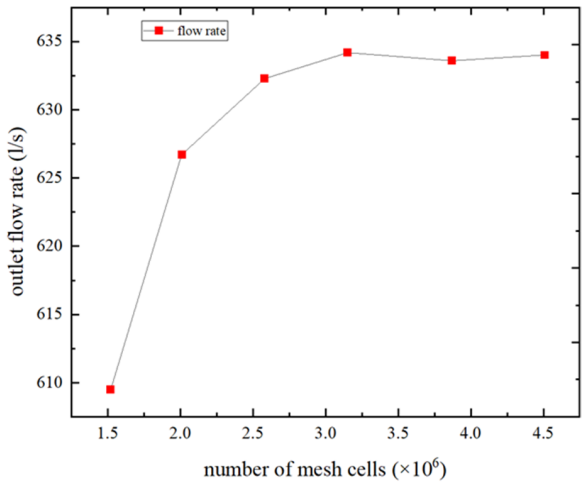

Figure 4. Mesh in dependence validation.

In this study, the transient operating conditions of the unit were simulated using the commercial software ANSYS Fluent, and unsteady numerical calculations were performed. The unsteady simulation was initialized using transient calculation conditions. The time step was set to 0.00036576 s, corresponding to a runner rotation of 3°. The number of iterations per time step ranged from 5 to 15. The rotor–stator interface was defined as Transient Rotor–Stator. The total simulation time was $30T_n$. The SST k-ω turbulence model was employed, as it is capable of accurately predicting flows with strong adverse pressure gradients and flow separation, making it suitable for capturing the complex flow structures in pump-turbines. The Zwart–Gerber–Belamri cavitation model, combined with the Mixture multiphase model, was adopted to capture the complex cavitating flow characteristics. At the initialization stage, the volume fraction of the liquid water phase was set to 1, while that of the water vapor phase was set to 0. A total pressure boundary condition was specified at the inlet, and a static pressure boundary condition was imposed at the outlet. All walls were defined as no-slip boundaries. The convergence criterion for the residuals was set to 1×10^{-5}. To verify the independence of the numerical results from the time step size, pressure pulsations in the vaneless region under the 22.5° guide vane opening condition were compared using time steps corresponding to runner rotations of 1°, 3°, and 6°, respectively. The results are shown in Figure 5. The pressure pulsation curves obtained with the three time steps exhibit generally consistent trends. However, in terms of peak prediction accuracy, the results corresponding to 1° and 3° per time step are significantly closer, while noticeable deviations are observed for the 6° time step. Considering both computational accuracy and efficiency, the time step corresponding to 3° runner rotation for the subsequent simulations.

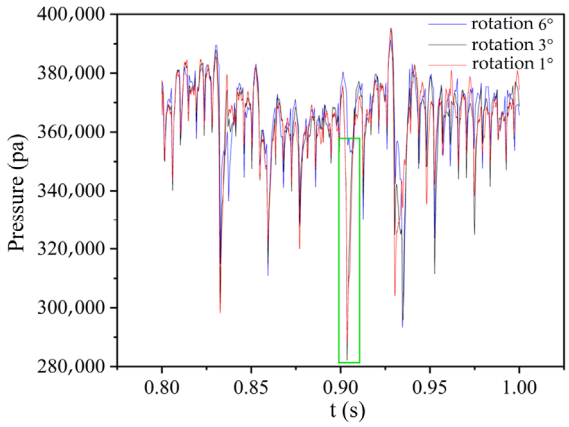

Figure 5. Time Step Independence Verification.

The arithmetic mean of the absolute errors for all operating points under the low-flow condition was defined as the average numerical error. As shown in Figure 6, the error of the standard k-ε model is nearly zero, while the errors of the other three models are 0.82%, 2.45%, and 2.45%, respectively. Considering factors such as the number of computational steps and convergence rate during the numerical simulation, the standard k-ε model exhibits better adaptability under the design condition. Under off-design conditions, certain discrepancies exist between numerical and experimental results. For large-flow conditions, the prediction errors of the four turbulence models increase with increasing flow rate. The head prediction errors of the k-ε and PANS models range from 2.65% to 11.94% and from 3.76% to 12.85%, respectively, and their head error curves show similar trends. The SST model yields head prediction errors ranging from 2.43% to 19.90%, with the error curve located at the uppermost position among the four models. The FBM model exhibits head prediction errors between 2.43% and 7.96%, and its error curve remains at the lowest position. These

results indicate that the SST model is more sensitive to operating condition variations under large-flow conditions, resulting in the largest prediction error. The *k*-ε and PANS models provide similar prediction accuracy, while the FBM model shows the best agreement with experimental data. From Figure 6 and Table 3, the maximum head prediction errors of the *k*-ε and SST models under low-flow conditions are 3.01% and 3.30%, respectively. The average head error and average efficiency error of both models are greater than those of the FBM model but smaller than those of the PANS model, and their head and efficiency error curves exhibit similar trends. This indicates that the *k*-ε and SST models provide relatively close predictions under low-flow conditions, with moderate accuracy. For the PANS model, the numerical error increases significantly as the flow rate decreases, with a maximum head prediction error of 11.19%. Both the average head error and the maximum head error are significantly larger than those of the other three models, indicating that the PANS model is more sensitive to operating condition variations under low-flow conditions and yields the largest error. In contrast, the FBM model shows an average head error of 1.19% and an average efficiency error of 5.31% under low-flow conditions, both of which are significantly lower than those of the other turbulence models. Therefore, the FBM model demonstrates higher accuracy for low-flow simulations of hydraulic machinery and shows good agreement with experimental data.

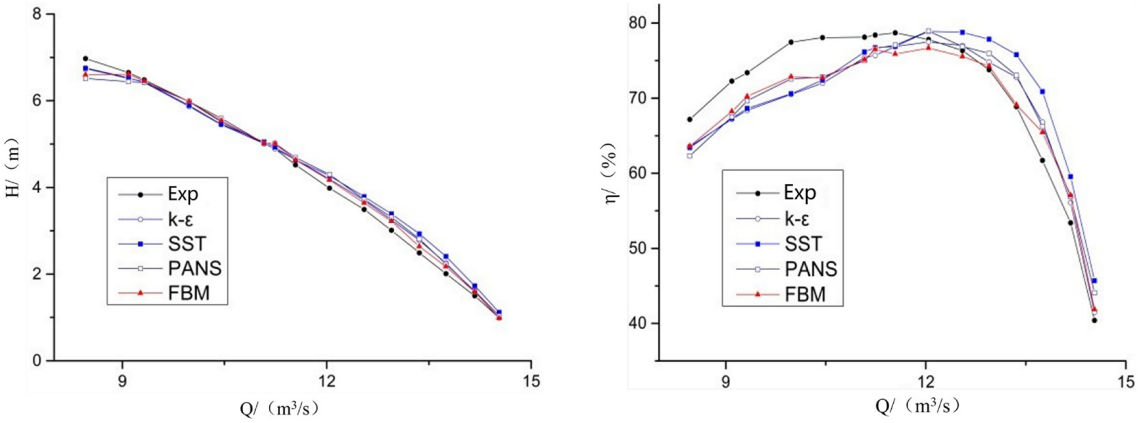

(**a**) *Q*-*H* curve (**b**) *Q*-*η* curve

Figure 6. Comparison of Predicted External Characteristics and Experimental Values.

Table 3. Average Numerical Errors for Different Turbulence Models at Low Flow Rates.

Turbulence Model	*k*-ε	SST	PANS	FBM
Average Relative Head Error/%	1.44	1.54	2.06	1.19
Average Efficiency Error/%	6.58	6.27	5.98	5.31

In summary, under the design condition, all four turbulence models can reasonably predict the external characteristics of the pump-turbine, with the standard *k*-ε model exhibiting relatively high accuracy. Under large-flow conditions, the SST model shows large fluctuations in prediction error and is strongly affected by operating condition variations, resulting in the lowest accuracy. The *k*-ε and PANS models provide similar prediction performance with moderate accuracy. Under low-flow conditions, the *k*-ε and SST models yield similar predictions with moderate accuracy, while the PANS model exhibits large error fluctuations and the lowest accuracy. Compared with the other three turbulence models, the FBM model produces the smallest prediction error, particularly under low-flow conditions, where it shows the best agreement with experimental data.

This study aims to investigate the transient flow characteristics within the draft tube under different operating conditions and their influence on the hydraulic load distribution of the runner. An unsteady numerical approach was employed to simulate the draft tube flow field, enabling the capture of dominant flow structures and time-dependent pressure characteristics under various load conditions. On this basis, the pressure fields at several typical instants were extracted and applied as equivalent hydraulic loads to the finite element model of the shaft system for structural analysis. The corresponding axial and radial equivalent stresses of the shaft were obtained, and the structural response characteristics under different load conditions were comparatively analyzed. Therefore, this study focuses on the variations in hydraulic loads induced by transient flow structures and their influence on the stress distribution and deformation characteristics of the shaft system.

3. Results

As the core energy conversion component of the pump-turbine unit, the internal flow condition of the runner directly affects the loading characteristics of the unit. To analyze the pressure distribution characteristics at different radial positions, several spanwise sections on the runner suction surface were selected for comparison.

To analyze the flow characteristics along the blade height, a dimensionless spanwise coordinate (Span) is defined, ranging from 0 to 1. Span = 0 corresponds to the crown (shroud), while Span = 1 corresponds to the hub. Typical spanwise sections at Span = 0.3, 0.6, and 0.9 are selected to represent the upper, middle, and lower regions of the blade, respectively.

On this basis, further analysis was conducted on the internal flow structures and pressure distribution characteristics of the unit under different operating conditions.

3.1. Pressure Distribution Characteristics in the Runner Flow Passage Under Different Operating Conditions

As the core component for energy conversion in the unit, the pressure distribution inside the runner passage directly affects the stress state of the runner. To analyze the pressure variation at different radial positions, several spanwise sections were selected on the runner suction surface for comparison, as shown in Figure 7.

As shown in Figure 7a, under the 70% load condition, obvious pressure gradients are observed on each spanwise section. A large low-pressure region appears near the suction surface of the blades and gradually expands along the flow passage direction, indicating significant flow non-uniformity inside the runner under this operating condition. As shown in Figure 7b, under the 100% load condition, the pressure distribution on each spanwise section is relatively uniform. The low-pressure region on the suction surface is significantly reduced, and the pressure contours are smooth, suggesting that the internal flow state of the runner is relatively stable. As shown in Figure 7c, under the 105% load condition, pressure non-uniformity reappears inside the runner flow passage. The low-pressure region locally expands, particularly in the outer spanwise region where the pressure gradient increases, indicating that overload operation affects the internal flow structure of the runner to some extent. Overall, the pressure distribution inside the runner flow passage shows a transition from highly non-uniform to relatively uniform with changing operating conditions. The pressure distribution is most non-uniform under the 70% load condition, while the flow field is the most stable under the 100% load condition. Under the 105% load condition, the local pressure gradient increases again. The flow recirculation and low-pressure regions induced by the draft tube vortex rope under low-flow conditions are important factors leading to uneven hydraulic loading on the runner.

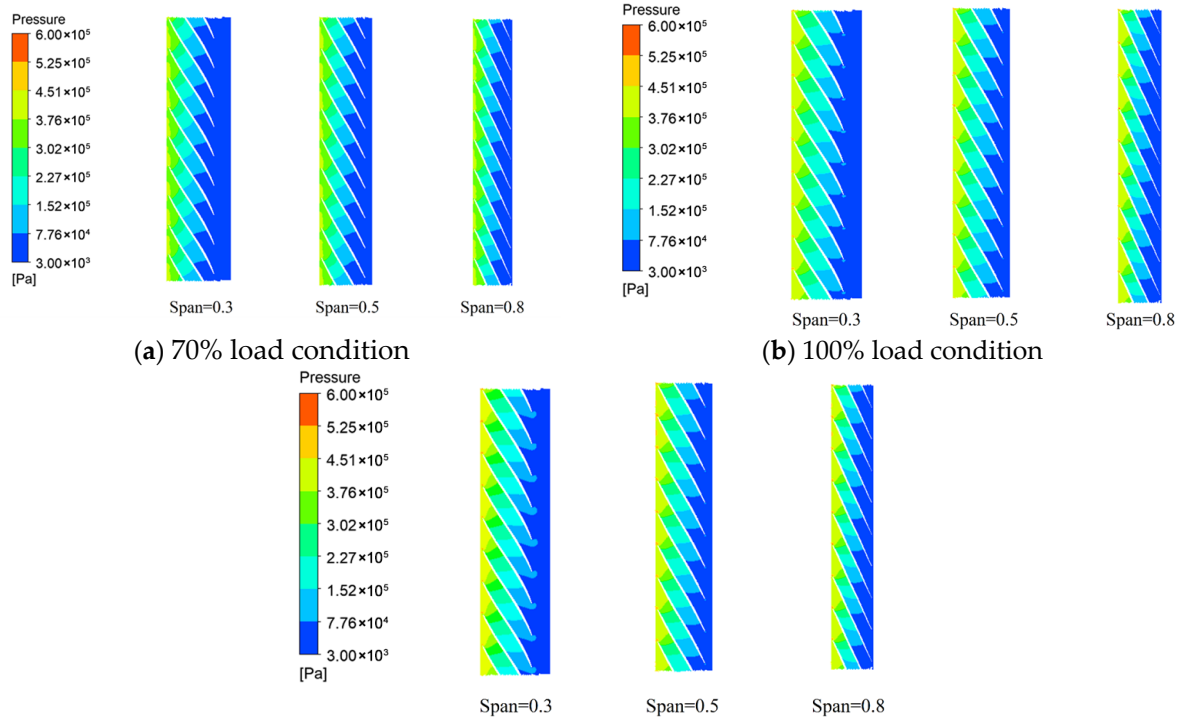

Figure 7. Pressure contour distributions on Span 0.3, Span 0.5, and Span 0.8 surfaces of the runner passages under different operating conditions.

3.2. Meridional Flow Structure in the Draft Tube

To analyze the internal flow structures of the unit under different operating conditions and their influence on runner loading, three representative load conditions of 70%, 100%, and 105% were selected for comparison. The flow field characteristics in the draft tube and the pressure distribution within the runner were evaluated based on unsteady numerical simulation results. Based on the obtained flow and pressure fields, the variation in hydraulic loading on the runner under different operating conditions was further examined.

As summarized in Table 4, significant differences in flow structure can be observed under different operating conditions, particularly in terms of symmetry and vortex development.

Table 4. Comparison of flow structure characteristics in the draft tube under different load conditions.

Load Condition	Flow Structure Feature	Symmetry	Vortex Characteristics
70%	Eccentric flow pattern	Strong asymmetry	Pronounced vortex rope, off-center
100%	Nearly axisymmetric	High symmetry	Weak vortex structure
105%	Central concentrated flow	Moderate asymmetry	Concentrated vortex in core region

A comparative analysis of the draft tube flow structures under 70%, 100%, and 105% load conditions is conducted to investigate the influence of operating load on the internal flow pattern. At 70% load (Figure 8a), the velocity distribution in the conical section of the draft tube exhibits pronounced circumferential asymmetry. The vortex core deviates from the geometric centerline, forming an eccentric spiral structure that extends downstream. A low-velocity region is concentrated on one side of the draft tube wall, while the opposite side maintains relatively higher velocity levels. This asymmetric flow pattern results in a non-uniform circumferential momentum distribution at the draft tube inlet. Under the rated condition (100%) (Figure 8b), the axisymmetry of the flow field is significantly enhanced. The high-velocity region is more uniformly distributed around the centerline, and the

vortex core approaches the geometric center. Compared with the 70% load condition, the low-velocity region near the wall is reduced. The circumferential velocity gradient decreases, and the overall flow structure becomes more balanced. At 105% load (Figure 8c), the flow structure differs from the other two conditions. A relatively concentrated axial vortex structure forms in the central region of the draft tube. Compared with the 70% load condition, the degree of circumferential asymmetry is weakened; however, the velocity magnitude in the central region increases. High-velocity flow is more concentrated near the center, while the near-wall velocity distribution becomes relatively uniform. A comparison of the three operating conditions indicates that the draft tube flow pattern exhibits a clear dependence on operating load. The part-load condition is characterized by eccentric spiral flow and strong circumferential non-uniformity. The rated condition shows the most symmetric and balanced velocity distribution. The overload condition presents a concentrated central vortex structure, with better circumferential symmetry than that observed under part-load operation. These differences in flow structure directly affect the pressure distribution at the runner outlet and provide a basis for the subsequent analysis of equivalent hydraulic loads.

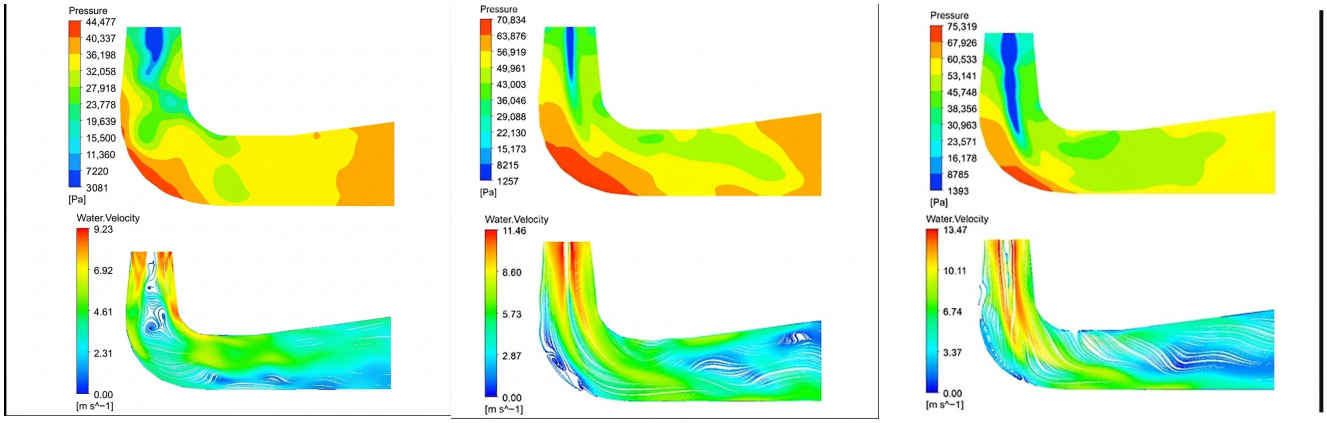

(**a**) 70%Pr (**b**) 100%Pr (**c**) 105%Pr

Figure 8. Pressure distribution and streamlines on the draft tube meridional plane under different operating conditions.

3.3. Pressure Distribution Characteristics on the Draft Tube Cross-Section

To further analyze the internal pressure field characteristics of the draft tube, three representative cross-sections located in the conical section at Z = −0.2, Z = −0.3 and Z = −0.4 m were selected to extract static pressure contours, as shown in Figure 9.

As shown in Table 5, the pressure distribution exhibits clear dependence on operating conditions, with the most uniform distribution at the rated condition and increased non-uniformity under off-design conditions.

Table 5. Comparison of pressure distribution characteristics at different load conditions.

Load Condition	Pressure Distribution	Circumferential Uniformity	Key Feature
70%	Highly non-uniform	Strong variation	Large pressure difference
100%	Most uniform	High uniformity	Balanced pressure field
105%	Moderately non-uniform	Intermediate	Increased pressure gradient

As shown in Figure 9a, under the 70% load condition, the pressure distribution on each cross-section exhibits pronounced circumferential asymmetry. The low-pressure region is concentrated on one side of the section, and the isobars deviate from the geometric center, forming an eccentric distribution pattern. Along the axial direction, this eccentric

feature remains evident across different sections, indicating significant circumferential non-uniformity of the sectional pressure field under this operating condition. As illustrated in Figure 9b, at the rated load condition (100%), the sectional pressure distribution approaches an axisymmetric pattern. The low-pressure region is primarily located near the center of the section, while the high-pressure region is more uniformly distributed along the circumferential direction. The isobars are approximately concentric. Compared with the 70% load condition, the circumferential pressure gradient is markedly reduced, and the pressure field becomes more balanced across all sections. Under the 105% load condition (Figure 9c), a certain degree of circumferential variation reappears in the sectional pressure distribution. The low-pressure region shifts relative to the rated condition, and the high-pressure region becomes intensified on one side of the section. As the section moves downstream, the circumferential pressure gradient gradually increases; however, the overall asymmetry remains weaker than that observed under the 70% load condition. A comprehensive comparison indicates that the sectional pressure field in the draft tube varies significantly with operating load. The part-load condition exhibits the most pronounced eccentric characteristics, the rated condition shows the most uniform pressure distribution, and the overload condition lies between the two. The circumferentially non-uniform distribution of sectional pressure directly affects the spatial distribution of hydraulic loads at the runner outlet, thereby providing a basis for the subsequent structural response analysis.

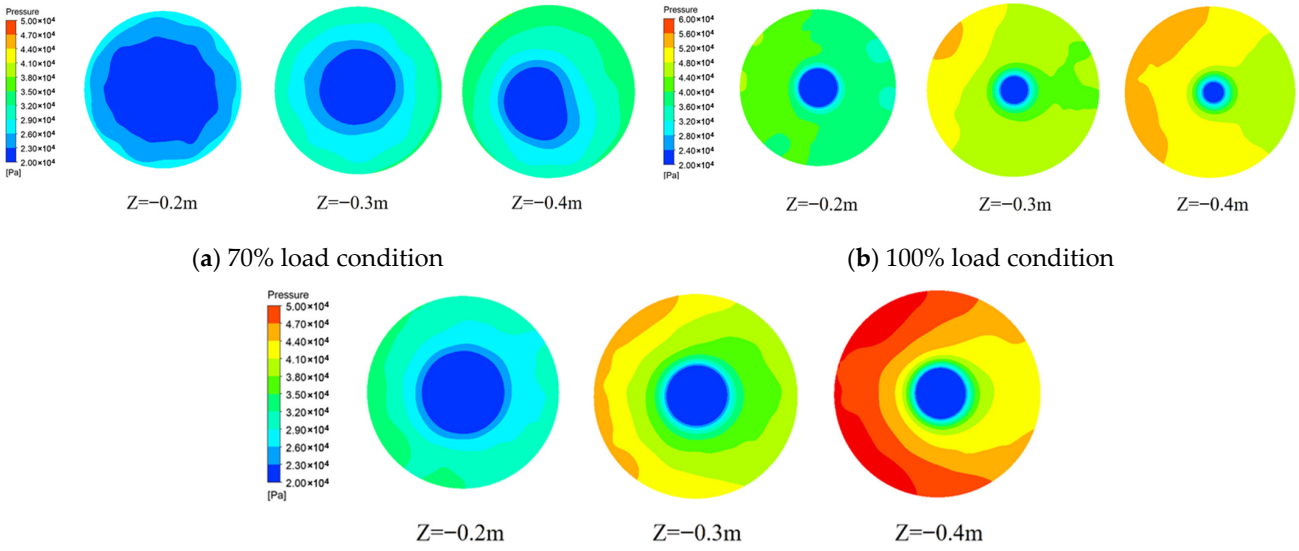

(**a**) 70% load condition (**b**) 100% load condition

(**c**) 105% load condition

Figure 9. Pressure distribution on the draft tube cross-section at different operating conditions.

3.4. Analysis of Spatial Morphological Characteristics of Draft Tube Vortex Rope Under Typical Operating Conditions

To further analyze the spatial distribution characteristics of vortex structures within the draft tube under different load conditions, the Q-criterion iso-surfaces were employed to identify the vortex structures based on the unsteady numerical simulation results. Figure 10 presents the three-dimensional morphology of the draft tube vortex rope under 70%, 100%, and 105% load conditions. As shown in Figure 10a, under the 70% load condition, a distinct spiral vortex rope structure can be identified within the conical section of the draft tube. The vortex rope extends downstream along the axial direction, and its central axis deviates from the geometric centerline of the draft tube, exhibiting a pronounced eccentric characteristic. In terms of spatial distribution, the vortex rope occupies a considerable volume within the conical section, and the overall structure presents significant non-axisymmetric features.

Combined with the previously discussed pressure distributions on the meridional and cross-sectional planes, it can be observed that strong circumferential non-uniformity exists in the flow field under this condition. As shown in Figure 10b, under the 100% load condition, the vortex rope structure inside the draft tube is significantly weakened. The Q-criterion iso-surfaces indicate that only small-scale vortex structures exist in the central region of the conical section. The overall spatial distribution tends toward axisymmetry, and no obvious eccentric phenomenon is observed. Compared with the 70% load condition, the vortex structure scale is markedly reduced, and the occupied spatial region becomes smaller, indicating a relatively stable flow field. As shown in Figure 10c, under the 105% load condition, a relatively large axial vortex structure appears in the central region of the draft tube. Compared with the 70% load condition, the eccentricity of the vortex rope is reduced, and its center is closer to the draft tube axis. However, the spatial scale of the vortex structure increases and is mainly concentrated in the central region of the conical section. Overall, the vortex rope under this condition exhibits a nearly axisymmetric distribution, although a certain degree of local non-uniformity can still be observed near the inlet region. A comprehensive comparison of the three operating conditions shows that the vortex rope is most pronounced and exhibits the strongest spatial asymmetry under the 70% load condition; it is weakest and the flow field is most uniform under the 100% load condition; while under the 105% load condition, the central vortex structure enlarges in scale but maintains better overall symmetry than that under 70% load. Variations in vortex rope morphology and spatial distribution under different load conditions directly affect the pressure distribution at the runner outlet, thereby leading to differences in the equivalent hydraulic loads acting on the runner.

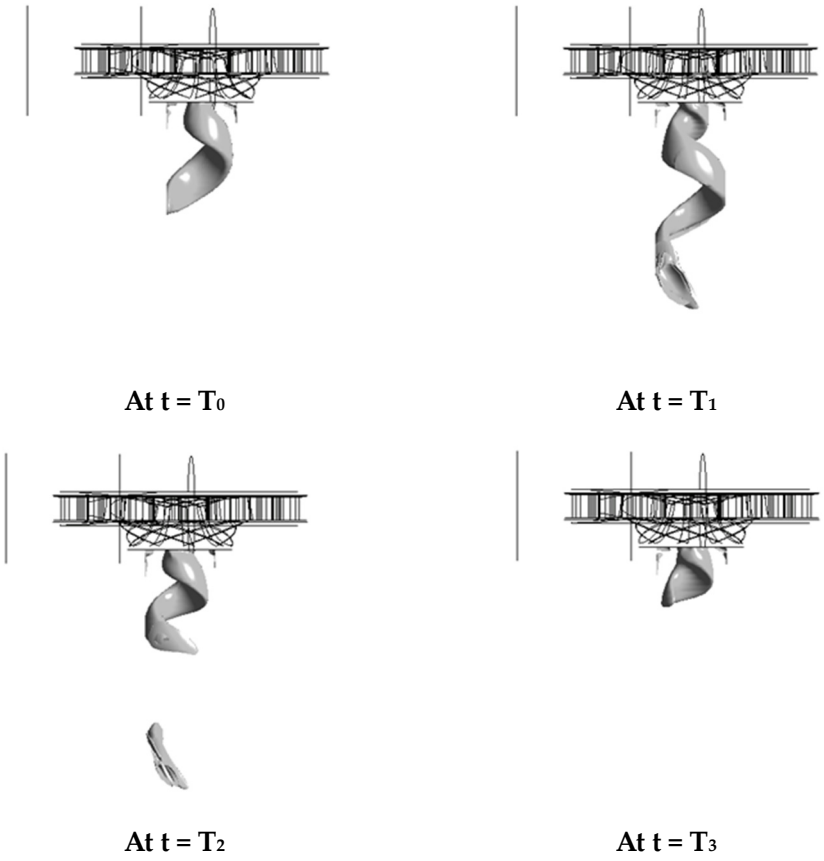

(**a**) 70% load condition

Figure 10. *Cont.*

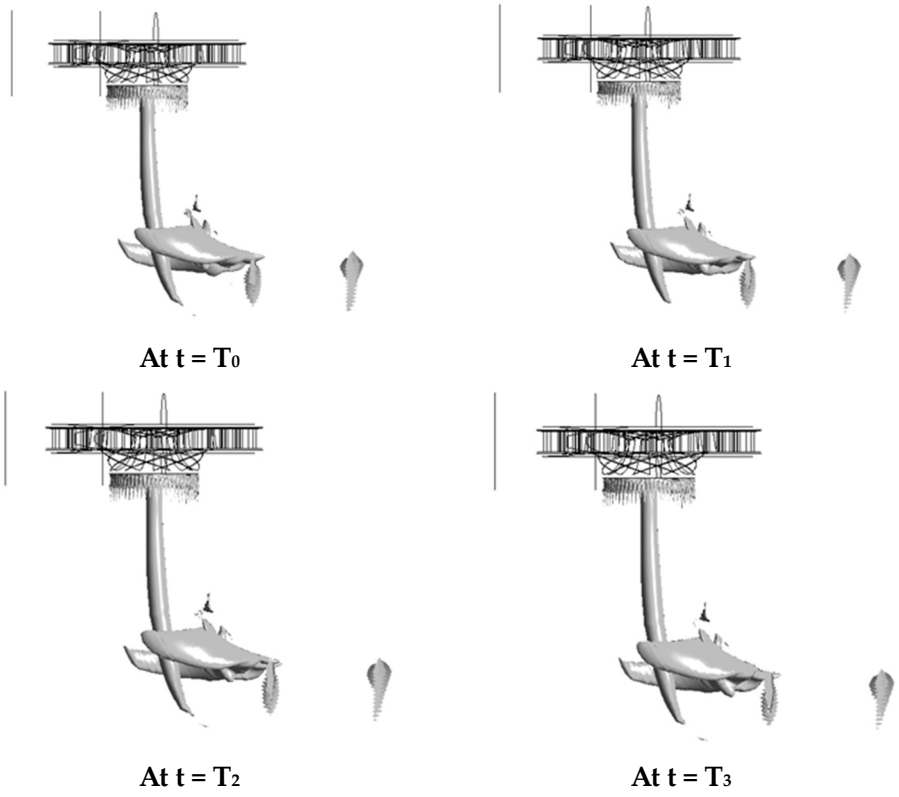

(**b**) 100% load condition

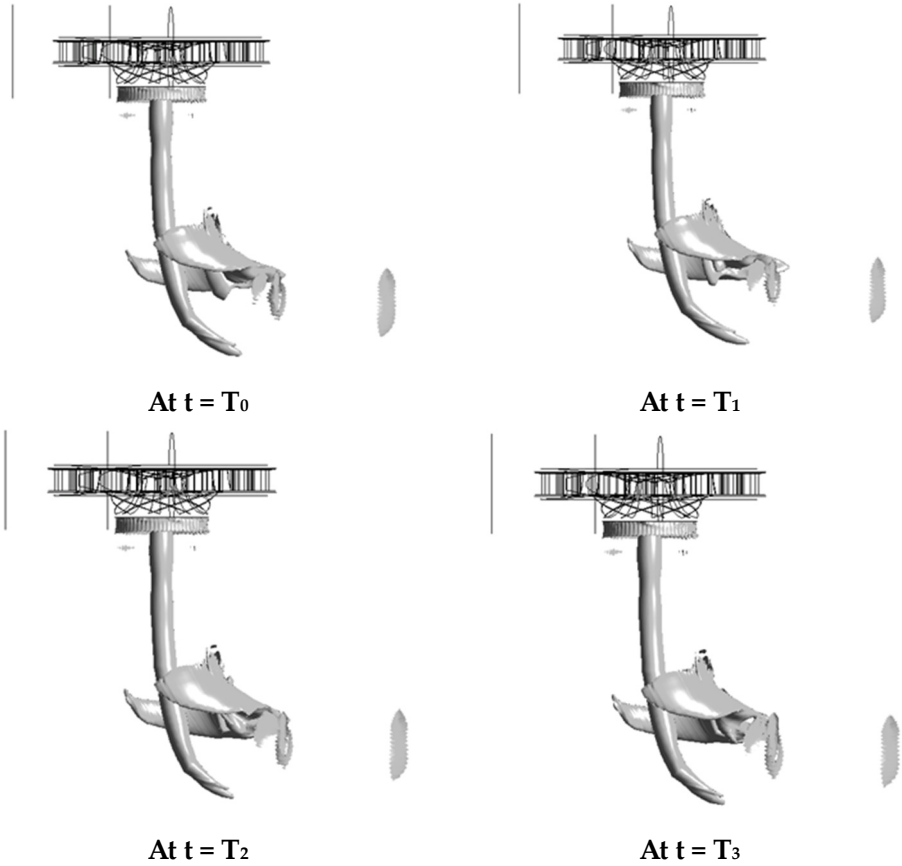

(**c**) 105% load condition

Figure 10. Three-dimensional structure of the draft tube vortex rope under different operating conditions based on the Q-criterion.

3.5. Pressure Pulsation Characteristics in the Draft Tube

To analyze the pressure pulsation characteristics within the draft tube and their axial and bend-region distribution patterns, multiple pressure monitoring points were arranged at representative locations in both the conical and bend sections of the draft tube, as shown in Figure 11. The monitoring points w_i2 and w_m2, as well as w_i3 and w_m3, are located on two horizontal sections at distances of 0.2 m and 0.4 m from the draft tube inlet, respectively. These points were used to compare the variations in pressure pulsation characteristics at different axial positions. The monitoring points w_i4, w_m4, and w_o4 are distributed in the bend section of the draft tube to analyze the pressure fluctuation behavior during flow turning and the associated spatial distribution differences. Through this arrangement of monitoring points, the evolution of pressure pulsations from the conical section to the bend region of the draft tube can be comprehensively characterized.

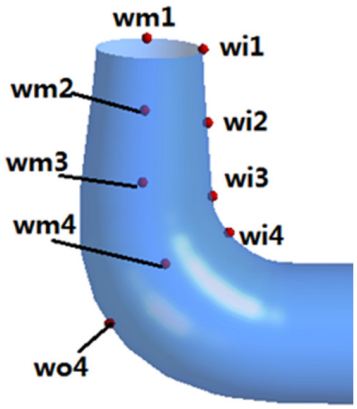

Figure 11. Distribution of monitoring points in the draft tube.

To facilitate frequency comparison under different operating conditions, the frequency was nondimensionalized. The horizontal axis was defined as the dimensionless frequency f/f_n, where f represents the frequency component of the pressure signal obtained through Fast Fourier Transform (FFT), and f_n denotes the rotational frequency of the runner. Since the rotational speed varies under different operating conditions, the use of dimensionless frequency eliminates the influence of rotational speed, thereby enabling a direct comparison of dominant frequency components and their harmonics.

The vertical axis is expressed in terms of the pressure pulsation coefficient C_p, which is defined as

$$C_p = \frac{P - \overline{P}}{\rho g H} \tag{10}$$

where P is the instantaneous pressure, $\overline{P}$ is the time-averaged pressure, and H denotes the hydraulic head. This dimensionless formulation eliminates the influence of differences in absolute pressure levels under various operating conditions, thereby enabling a comparable evaluation of pressure fluctuation intensity.

By performing frequency-domain analysis of the pressure time-history signals at the monitoring points, the amplitude and dominant frequency characteristics of pressure pulsations in the draft tube under different load conditions can be identified. Furthermore, the relationship between variations in vortex rope structures and the corresponding pressure fluctuation characteristics can be elucidated.

The dominant frequencies at different monitoring points were identified based on the peak values in the frequency spectra. As summarized in Table 6, two main types of frequency components can be distinguished. The low-frequency components ($f/f_n \approx 0.2$–0.4) correspond to the precession frequency of the draft tube vortex rope, while the components

near $f/f_n \approx 1$ are associated with the runner rotational frequency. The results indicate that the vortex rope frequency dominates the pressure pulsation characteristics under off-design conditions. Furthermore, the identified dominant frequency was compared with the well-established scaling law of draft tube vortex rope precession. Previous studies have reported that the vortex rope frequency typically falls within the range of 0.2–0.4f_n under part-load conditions. The present results show that the dominant low-frequency component is approximately 0.25–0.30f_n, which agrees well with the reported range. This consistency indicates that the observed pressure pulsations are primarily governed by the precessing vortex rope in the draft tube.

Table 6. Dominant frequencies of pressure pulsations at different monitoring points.

Monitoring Point	Dominant Frequency (f/f_n)	Physical Interpretation
w_i2	0.25–0.30	Vortex rope frequency
w_m2	0.25–0.30	Vortex rope frequency
w_i3	0.25–0.30	Vortex rope frequency
w_m3	0.25–0.30	Vortex rope frequency
w_i4	0.25–0.30	Vortex rope frequency
w_m4	0.25–0.30	Vortex rope frequency
w_o4	0.25–0.30	Vortex rope frequency
All points	1.0	Runner rotational frequency

Figure 12 presents the pressure pulsation spectra at various monitoring points in the draft tube under 70%, 100%, and 105% load conditions. The horizontal axis represents the dimensionless frequency f/f_n, while the vertical axis denotes the pressure pulsation coefficient C_p. It should be noted that the original frequency analysis range was f/f_n = 0–30. However, based on the updated figure, it can be observed that in the frequency range of $f/f_n > 6$, the spectral amplitudes at all monitoring points are close to zero, and no distinct peaks or energy concentration can be identified. This frequency range contributes little to the characterization of the dominant pressure pulsation features. Therefore, in order to more clearly highlight the spectral characteristics within the dominant frequency range and improve the effectiveness of the graphical representation, the subsequent analysis focuses on the frequency range of f/f_n = 0–6.

Under the 70% load condition, the pressure pulsation energy at all monitoring points is mainly concentrated in the low-frequency region. The dominant peaks are distributed within $f/f_n < 5$, primarily located in the range of $f/f_n \approx$ 1–3. According to the scale shown in the figure, the peak value of the pressure pulsation coefficient is approximately $C_p \approx 0.004$–0.006. As the frequency increases, the spectral amplitude decreases rapidly, and beyond $f/f_n > 6$, almost no significant energy distribution is observed, with no evident secondary peaks. Differences in peak amplitudes exist among monitoring points, with slightly higher values in the bend section compared to the conical section, while the dominant frequency locations remain consistent. Combined with the previously presented vortex morphology analysis, an eccentric spiral vortex rope exists under this condition, corresponding to relatively high low-frequency pressure pulsation amplitudes and noticeable spatial non-uniformity.

Under the 100% load condition, the overall spectral distribution remains similar to that under the 70% load condition. The pressure pulsation energy is still mainly concentrated in the region of $f/f_n < 5$, and the dominant frequency range remains at $f/f_n \approx$ 1–3. The peak amplitude is approximately $C_p \approx 0.003$–0.005, which is lower than that under the 70% load condition. In the frequency range of $f/f_n > 6$, the spectral amplitude also decreases rapidly without any noticeable enhancement, indicating that the high-frequency components contribute little to the overall pressure pulsation. Although slight amplitude differences

can still be observed among monitoring points at different axial positions, the overall spectral structure does not change significantly. In combination with the vortex morphology results, the flow field tends to become more axisymmetric with a reduced vortex scale, corresponding to a lower overall pressure pulsation level and a more uniform and stable energy distribution.

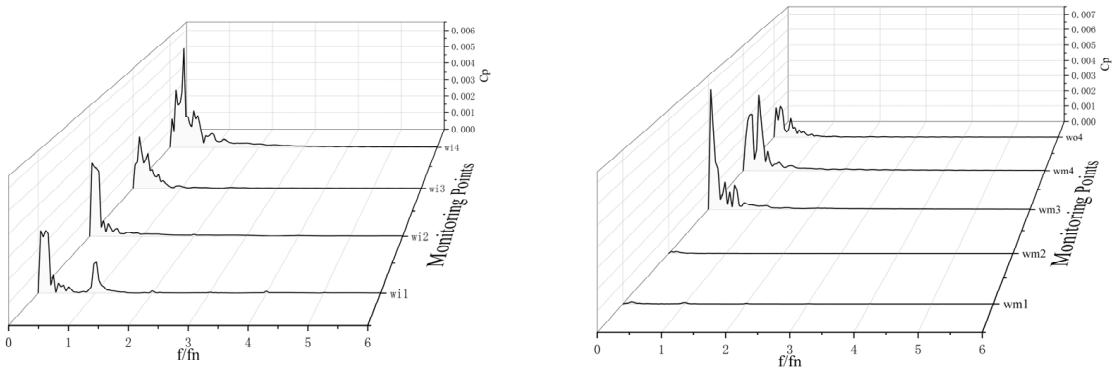

(**a**) Pressure Pulsation at Monitoring Points in the Draft Tube under 70% Load

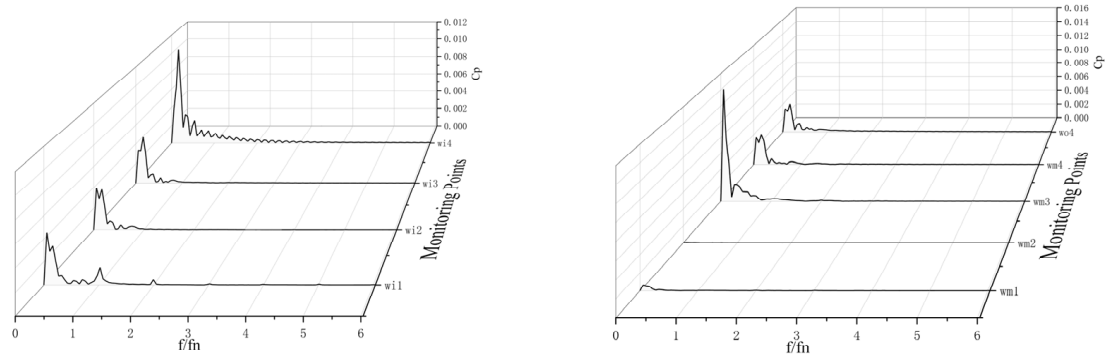

(**b**) Pressure Pulsation at Monitoring Points in the Draft Tube under 100% Load

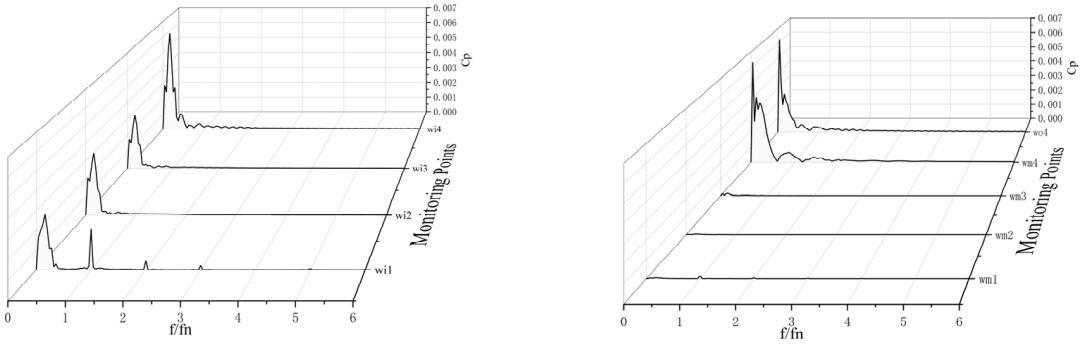

(**c**) Pressure Pulsation at Monitoring Points in the Draft Tube under 105% Load

Figure 12. Pressure pulsation characteristics at draft tube monitoring points under different load conditions.

Under the 105% load condition, the pressure pulsation spectrum is still dominated by low-frequency components, with the dominant peaks remaining within $f/f_n < 5$ and no

significant shift in the dominant frequency. According to the figure, the peak amplitudes at some monitoring points increase significantly, reaching approximately $C_p \approx 0.010$–0.014, which is considerably higher than those under the 70% and 100% load conditions. In the range of $f/f_n > 6$, the spectral amplitude remains low and no new high-frequency peaks appear, indicating that the high-frequency structure does not undergo significant changes. Overall, the spectral structure remains consistent, and the primary variation is reflected in the significant increase in low-frequency amplitudes. Combined with the vortex morphology analysis, a relatively large-scale axial vortex structure is observed in the central region of the draft tube under this condition, corresponding to a marked enhancement in low-frequency pressure pulsation intensity while the frequency distribution remains stable.

A comparison of the three operating conditions indicates that pressure pulsations in the draft tube are consistently dominated by low-frequency components ($f/f_n < 5$), while the spectral energy in the higher frequency range ($f/f_n > 6$) decays rapidly without forming effective peak structures, suggesting a limited contribution of high-frequency components to the overall pulsation characteristics. The dominant frequency positions remain nearly unchanged across different load conditions, indicating that the characteristic frequency structure of the flow system is relatively stable, whereas variations in operating conditions mainly affect the amplitude level of pressure pulsations. Among the three conditions, the lowest amplitude occurs at 100% load, followed by 70% load, while the highest amplitude is observed at 105% load. In conjunction with the spatial morphology of the vortex rope, it can be further inferred that variations in vortex scale and symmetry primarily modulate the intensity of pressure pulsations, while having a limited influence on the dominant frequency distribution. Larger-scale or more unstable vortex structures are generally associated with higher low-frequency pressure pulsation amplitudes.

3.6. Equivalent Stress Distribution of the Blade Under Various Operating Loads

Figure 13 presents the equivalent stress distributions of the runner blades under 70%, 100%, and 105% load conditions. The results are obtained based on steady hydraulic loads. Under the 70% load condition, as shown in Figure 13a, the maximum equivalent stress is 2.98 MPa. The stress concentration is mainly located near the blade inlet region. Most areas of the blade maintain relatively low stress levels, and no continuous high-stress band similar to that observed under the rated condition is identified. Under the rated load condition (100%), as shown in Figure 13b, the maximum equivalent stress increases significantly to 9.51 MPa, which is approximately 3.8 times that under the 105% load condition. Compared with the other two conditions, a continuous high-stress region appears near the blade outlet on the rim side. The area of medium-to-high stress expands markedly, and the stress distribution is no longer confined to the local inlet region but extends toward the outlet. Under the 105% load condition, as shown in Figure 13c, the maximum equivalent stress is 2.49 MPa. The high-stress region is mainly concentrated locally near the blade inlet on the rim side. Most areas of the blade exhibit relatively low stress levels, predominantly ranging from blue to green. The stress gradient along the blade span is relatively smooth, and no large continuous high-stress band is observed.

Overall, although the rated condition exhibits the highest stress peak, the stress distribution is more uniform. In contrast, the 70% load condition shows lower peak stress but more pronounced local concentration and asymmetry. Both the 105% and 70% load conditions are characterized by local stress concentration near the blade inlet. These results indicate that under unsteady hydraulic loading, the structural response of the runner blade exhibits a clear dependence on the operating condition.

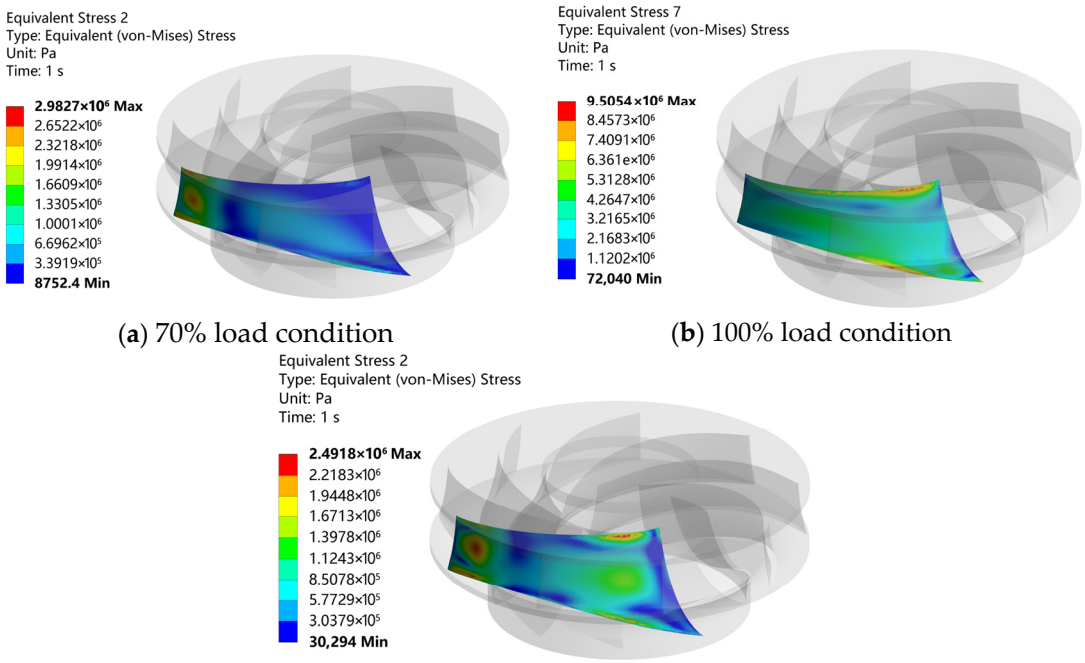

(**a**) 70% load condition (**b**) 100% load condition

(**c**) 105% load condition

Figure 13. Equivalent Stress Distribution of the Blade under Different Loads.

3.7. Different Load Conditions on Static Stress of Shafting and Deformation Characteristics of the Runner

The variation in blade stress distribution under different load conditions reflects the changes in hydraulic loading characteristics at the runner outlet. In particular, under the rated load condition, a more extensive and pronounced high-stress region is observed near the blade outlet, indicating that the hydraulic forces in this area are more concentrated and unevenly distributed. Since the runner outlet flow directly determines the inlet flow condition of the draft tube, the non-uniform distribution of hydraulic loads near the blade outlet may influence the circumferential velocity field entering the draft tube. Differences in the outlet flow pattern may further affect the formation and evolution of downstream flow structures. Consequently, the steady hydraulic excitation transmitted to the shaft system is also expected to vary with the operating condition. This analysis provides a structural-level interpretation for the subsequent discussion of load-dependent shaft system responses.

After obtaining the equivalent hydraulic loads on the runner under different operating conditions, the loads were applied to the finite element model of the shaft system to conduct static structural analysis. The equivalent stress distribution of the shaft system and the overall deformation characteristics of the runner were obtained. Figures 14 and 15 show the shaft stress contours and runner deformation contours under 70%, 100%, and 105% load conditions, respectively.

(1) 70% Load Condition

As shown in Figures 14a and 15a, the maximum equivalent stress of the shaft system is 3.1901 MPa under 70% load. The equivalent stress is mainly concentrated in the transition region between the runner rim and the main shaft, where obvious local stress concentration occurs. Combined with the previous flow field analysis, an eccentric helical vortex rope is observed in the draft tube under this operating condition, leading to significant circumferential flow asymmetry. The overall runner deformation is dominated by axial displacement, with a maximum deformation of approximately 0.009195 mm. Meanwhile, a certain degree of radial deviation can be observed at the runner rim. The maximum

deformation region is mainly located near the blade outlet, corresponding to regions with large pressure gradients.

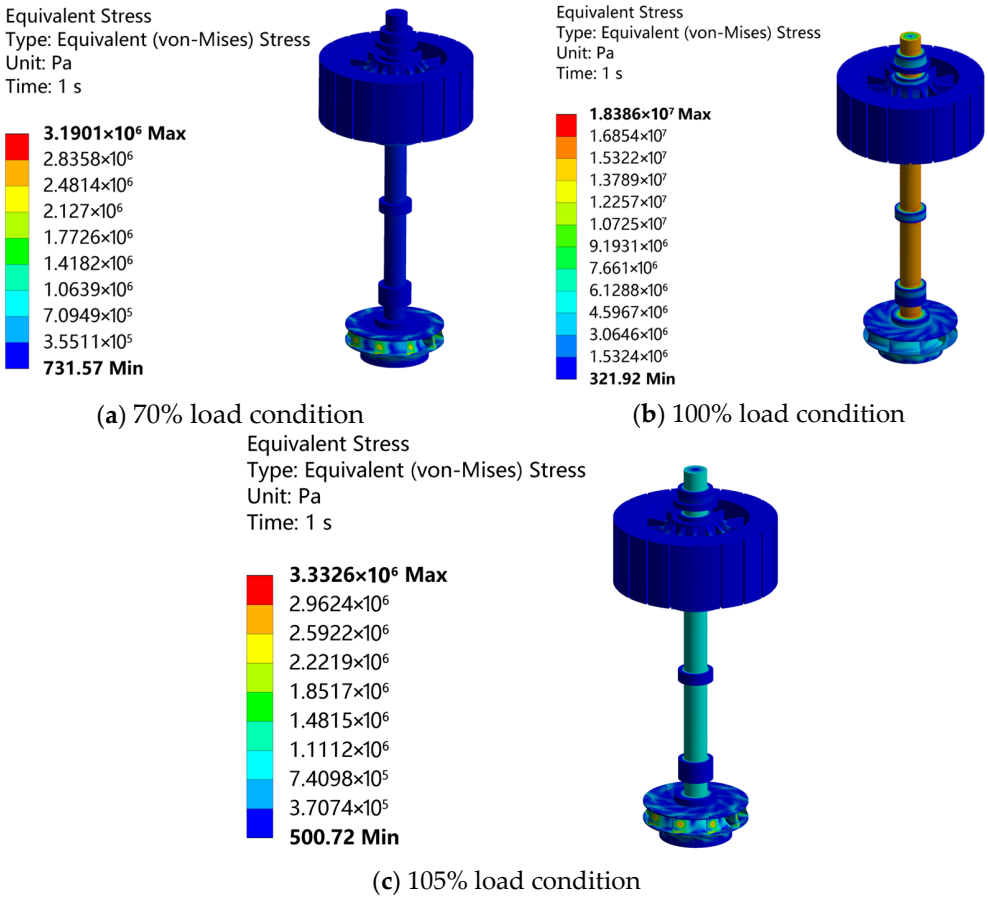

(**a**) 70% load condition (**b**) 100% load condition

(**c**) 105% load condition

Figure 14. Distribution of shaft stress under different load conditions.

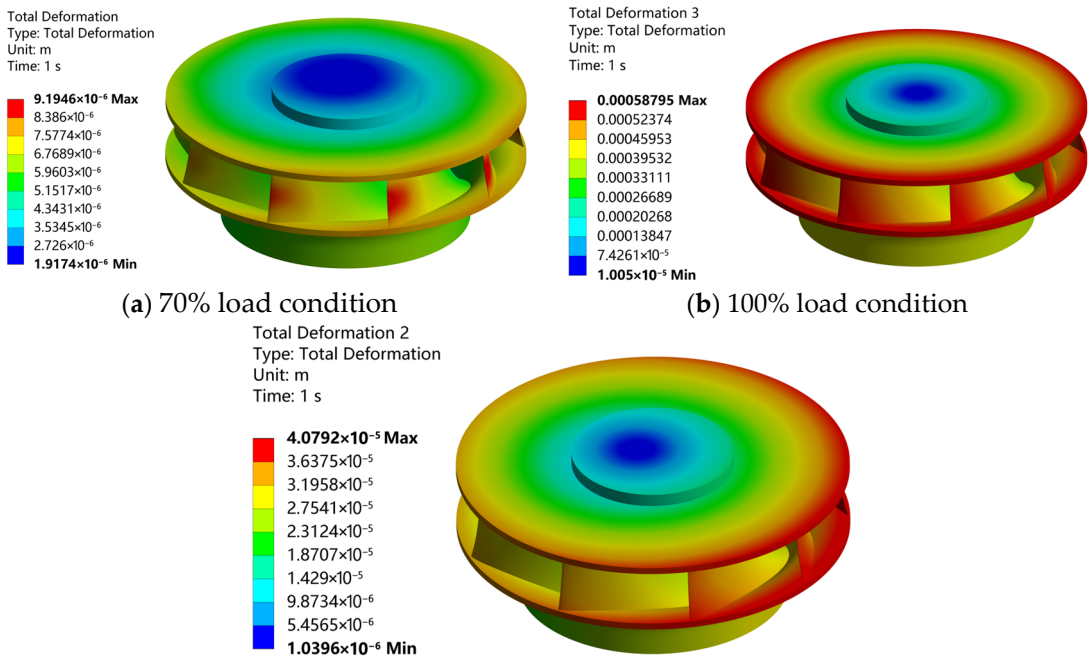

(**a**) 70% load condition (**b**) 100% load condition

(**c**) 105% load condition

Figure 15. Total deformation contours of the runner under different load conditions.

(2) 100% Load Condition

As shown in Figures 14b and 15b, the maximum equivalent stress is 1.8386 MPa under 100% load. The overall stress level is significantly reduced, and the stress distribution is relatively uniform without obvious local stress concentration. The maximum deformation value is approximately 0.0005879 mm, indicating a relatively small deformation amplitude. The overall deformation distribution is nearly axisymmetric, and no obvious eccentric deformation region is observed. These results are consistent with the weakened vortex structure and more uniform flow field characteristics in the draft tube.

(3) 105% Load Condition

As shown in Figures 14c and 15c, the maximum equivalent stress is 3.3326 MPa under 105% load. The stress level is significantly higher than that under the rated condition (100% load), increasing from 1.8386 MPa to 3.3326 MPa, which corresponds to an increase of approximately 81%, but the overall distribution remains relatively continuous. The stress concentration region is still mainly located at the transition zone between the runner rim and shaft. The maximum deformation is approximately 0.0041 mm. Although the overall deformation amplitude is larger than that at the rated condition, the spatial distribution remains relatively uniform without obvious eccentric concentration. Compared with the 70% load condition, the vortex structure in the central region is less eccentric, resulting in better axial symmetry of structural response.

Comparison of the three operating conditions shows that the stress level is highest and the structural response is most non-uniform at 70% load. The stress and deformation amplitudes are lowest at 100% load. At 105% load, the structural response is significantly enhanced compared with the rated condition, but the overall symmetry is better than that at 70% load. The differences in draft tube flow structures under different loads lead to variations in the pressure distribution on the runner surface, thereby causing differences in the static mechanical response of the shaft system. These results indicate that variations in draft tube flow structures have a significant influence on shaft stress levels and runner deformation behavior.

3.8. Relationship Between Draft Tube Pressure Asymmetry and Shaft System Stress Distribution

By comparing the pressure distribution results presented in Section 3 with the structural response results in this section, a clear correspondence can be identified between flow field asymmetry and the stress characteristics of the shaft system. Under the 70% load condition, the pressure field on the draft tube cross-section exhibits a pronounced circumferential non-uniform distribution, with the low-pressure region deviating from the geometric center. This asymmetric pressure field leads to a non-uniform radial hydraulic load distribution at the runner outlet, thereby inducing a more significant bending tendency in the shaft system. Accordingly, the equivalent stress and deformation levels under this condition are relatively higher. Under the 100% rated condition, the pressure field approaches an axisymmetric distribution, and the circumferential pressure gradient is reduced, resulting in a more uniform circumferential load acting on the runner. The corresponding structural response of the shaft system is more balanced, with the lowest stress concentration and deformation magnitude among the three operating conditions. Under the 105% load condition, although certain circumferential differences in pressure distribution are still present, the degree of asymmetry is lower than that under the partial load condition. Therefore, the hydraulic load distribution and structural response characteristics fall between those observed at 70% and 100% load conditions. These results indicate that the circumferential non-uniformity of the draft tube pressure field directly influences the spatial distribution of hydraulic loads at the runner outlet, thereby determining the mechanical state of the shaft system.

4. Discussion

Transient simulations show that load variation significantly alters the flow organization in the draft tube, which directly affects hydraulic load distribution. Under 70% load, a pronounced eccentric vortex structure leads to strong circumferential asymmetry and increased low-frequency pressure pulsation ($C_p \approx 0.004$–0.006). At the rated condition, the flow becomes more axisymmetric with reduced pulsation intensity ($C_p \approx 0.003$–0.005). Under 105% load, a concentrated central vortex forms, accompanied by a significant increase in pulsation amplitude ($C_p \approx 0.010$–0.014).

The dominant frequency remains stable at $f/f_n \approx 0.25$–0.30 across all conditions, indicating that load variation mainly affects pulsation amplitude rather than frequency characteristics. The attenuation of pulsation along the axial direction suggests energy dissipation, while the bend region shows higher sensitivity due to geometric effects.

The structural analysis indicates that stress is concentrated at the runner–shaft junction and transition regions. Although the stress distribution pattern remains similar, the magnitude varies significantly with operating conditions. The maximum equivalent stress increases from 1.8386 MPa at 100% load to 3.3326 MPa at 105% load (≈81% increase), while the deformation reaches its maximum at 70% load (0.009195 mm), reflecting the influence of strong flow asymmetry.

Overall, vortex evolution is identified as the key factor linking flow non-uniformity and shaft mechanical response, establishing a quantitative flow–load–structure relationship.

It should be noted that the present study has several limitations, including the use of one-way FSI, equivalent static structural analysis, limited operating conditions, and incomplete experimental validation. Therefore, the conclusions are mainly applicable to comparative analysis under typical operating conditions.

Comparison with previous studies (Table 7) shows that the dominant frequency agrees with the commonly reported range (0.2–$0.4f_n$). However, structural response is rarely addressed in existing research. This study extends previous work by quantitatively linking flow asymmetry with structural response, providing additional insight into flow–structure coupling mechanisms.

Table 7. Comparison of the present study with previous studies on draft tube vortex rope and structural response.

Study	Method	Operating Condition	Dominant Frequency	Structural Response	Key Findings
Ref. [3]	Exp + CFD	Part-load	0.2–$0.4f_n$	Not reported	Vortex rope induces low-frequency pulsation
Ref. [6]	Exp	Variable load	0.2–$0.35f_n$	Not reported	Precession linked to swirl number
Ref. [8]	LES	Transient condition	~$0.3f_n$	Not reported	Detailed vortex evolution resolved
Ref. [13]	CFD	Low flow	-	Not considered	Rotor–stator interaction enhances pulsation
This study	CFD + FSI	70%, 100%, 105% load	0.25–$0.30f_n$	1.84–3.33 MPa	Flow–load–structure relationship established

It should be noted that most previous studies mainly focus on flow characteristics and pressure pulsations, while structural response is rarely reported.

5. Conclusions

Transient flow simulations and equivalent structural analyses were performed under 70%, 100%, and 105% load conditions to investigate the relationship between draft tube vortex structures and shaft system mechanical response. The main conclusions are as follows:

(1) Distinct flow structures are observed under different load conditions. At 70% load, the draft tube flow exhibits the strongest circumferential asymmetry and the most pronounced eccentric vortex structure. At 100% load, the flow field is closest to axisymmetric and the pressure distribution is the most uniform. At 105% load, a concentrated vortex structure forms in the central region of the draft tube, and the degree of circumferential non-uniformity lies between those under 70% and 100% load conditions.

(2) Pressure pulsation characteristics show clear load dependence. Under all three operating conditions, the dominant pressure pulsation energy is mainly concentrated in the low-frequency range. The peak pressure pulsation coefficient is approximately 0.004–0.006 at 70% load, 0.003–0.005 at 100% load, and 0.010–0.014 at 105% load. Therefore, the rated condition exhibits the lowest pulsation intensity, while the overload condition shows the highest low-frequency pulsation level.

(3) The mechanical response of the shaft system differs significantly under different operating conditions. The maximum equivalent stress of the shaft system is 3.1901 MPa at 70% load, 1.8386 MPa at 100% load, and 3.3326 MPa at 105% load. The corresponding maximum runner deformations are approximately 0.009195 mm, 0.0005879 mm, and 0.0041 mm, respectively. Compared with the rated condition, the maximum stress under 105% load increases by approximately 81%, while the deformation under 70% load is the largest among the three conditions.

(4) Variations in draft tube vortex structures and pressure distributions directly affect the hydraulic load distribution at the runner outlet, thereby influencing the stress and deformation characteristics of the shaft system. Among the three operating conditions, the rated condition shows the most balanced flow field and the lowest structural response level, whereas off-design conditions lead to stronger flow non-uniformity and higher stress or deformation levels. These results confirm that draft tube flow asymmetry is an important hydrodynamic factor governing shaft system mechanical response.

The present study is limited to a one-way fluid–structure interaction framework and equivalent static structural analysis under three typical load conditions. Future work will focus on two-way fluid–structure interaction, a wider range of operating conditions, and further experimental validation, so as to better clarify the dynamic mechanical behavior of pump-turbine shaft systems under complex operating scenarios.

Author Contributions: Conceptualization, Y.L.; methodology, L.C.; validation, A.Y. and L.D.; formal analysis, A.Y.; investigation, Y.L.; data curation, L.D.; writing—original draft preparation, Y.L. and L.D.; writing—review and editing, A.Y.; supervision, A.Y.; project administration, A.Y.; funding acquisition, A.Y. All authors have read and agreed to the published version of the manuscript.

Funding: This research was funded by Shanghai Investigation, Design & Research Institute Co., Ltd. (No. 2022SD(83)-010). The authors declare that this study received funding from Shanghai Investigation, Design & Research Institute Co., Ltd. The funder had the following involvement with the study: funding acquisition and project support.

Data Availability Statement: The original contributions presented in this study are included in the article. Further inquiries can be directed to the corresponding author.

Conflicts of Interest: Author Yanhao Li is employed by Shanghai Investigation, Design & Research Institute Co., Ltd. The remaining authors declare no conflict of interest.

References

1. Ruprecht, A.; Helmrich, T.; Aschenbrenner, T.; Scherer, T. Simulation of vortex rope in a turbine draft tube. In Proceedings of the 21th Symposium IAHR on Hydraulic Machinery and Systems, Lausanne, Switzerland, 9–12 September 2002; EPFL: Lausanne, Switzerland, 2022; pp. 259–266.
2. Kirschner, O.; Ruprecht, A.; Göde, E.; Riedelbauch, S. Experimental investigation of pressure fluctuations caused by a vortex rope in a draft tube. In Proceedings of the IOP Conference Series: Earth and Environmental Science, Beijing, China, 19–23 August 2012; IOP: London, UK, 2012; p. 062059.
3. Muntean, S.; Tănasă, C.; Bosioc, A.; Moş, D. Investigation of the plunging pressure pulsation in a swirling flow with precessing vortex rope in a straight diffuser. In Proceedings of the IOP Conference Series: Earth and Environmental Science, Prague, Czech Republic, 5–9 September 2016; IOP: London, UK, 2016; p. 082010.
4. Skripkin, S.; Tsoy, M.; Kuibin, P.; Shtork, S. Study of pressure shock caused by a vortex ring separated from a vortex rope in a draft tube model. *J. Fluids Eng.* **2017**, *139*, 081103. [CrossRef]
5. Cheng, H.; Zhou, L.; Liang, Q.; Guan, Z.; Liu, D.; Wang, Z.; Kang, W. A method of evaluating the vortex rope strength in draft tube of Francis turbine. *Renew. Energy* **2020**, *152*, 770–780. [CrossRef]
6. Favrel, A.; Gomes Pereira Junior, J.; Landry, C.; Müller, A.; Nicolet, C.; Avellan, F. New insight in Francis turbine cavitation vortex rope: Role of the runner outlet flow swirl number. *J. Hydraul. Res.* **2018**, *56*, 367–379. [CrossRef]
7. Sotoudeh, N.; Maddahian, R.; Cervantes, M.J. Investigation of rotating vortex rope formation during load variation in a Francis turbine draft tube. *Renew. Energy* **2020**, *151*, 238–254. [CrossRef]
8. Jin, F.; Li, P.; Tao, R.; Xiao, R.; Zhu, D. Study of vortex rope for the flow field pulsation law. *Ocean Eng.* **2023**, *273*, 114026. [CrossRef]
9. Li, P.; Lu, J.; Tao, R.; Xiao, R.; Ji, B.; Wang, F. Energy distribution and chaotic pressure pulsation analysis of vortex ropes in Francis-99. *Eng. Appl. Comput. Fluid Mech.* **2024**, *18*, 2310609. [CrossRef]
10. Susan-Resiga, R.; Vu, T.C.; Muntean, S.; Ciocan, G.D.; Nennemann, B. Jet control of the draft tube vortex rope in Francis turbines at partial discharge. In Proceedings of the 23rd IAHR Symposium Conference, Ann Arbor, MI, USA, 31 May–3 June 2006; IAHR: Madrid, Spain, 2006; pp. 67–80.
11. Shtork, S.; Suslov, D.; Skripkin, S.; Litvinov, I.; Gorelikov, E. An overview of active control techniques for vortex rope mitigation in hydraulic turbines. *Energies* **2023**, *16*, 5131. [CrossRef]
12. Lai, X.-D.; Liang, Q.-W.; Ye, D.-X.; Chen, X.-M.; Xia, M.-M. Experimental investigation of flows inside draft tube of a high-head pump-turbine. *Renew. Energy* **2019**, *133*, 731–742. [CrossRef]
13. Kim, S.-J.; Suh, J.-W.; Choi, Y.-S.; Park, J.; Park, N.-H.; Kim, J.-H. Inter-blade vortex and vortex rope characteristics of a pump-turbine in turbine mode under low flow rate conditions. *Water* **2019**, *11*, 2554. [CrossRef]
14. He, Q.; Huang, X.; Bi, H.; Yang, M.; Yang, H.; Wang, Z. Draft tube vortex rope analysis of a pump-turbine unit under different operating conditions. In *Proceedings of the IOP Conference Series: Earth and Environmental Science*; IOP: London, UK, 2022; p. 012012.
15. Xin, L.; Li, Q.; Zhang, S. Coupling Mechanisms Between Vortex Rope Evolution and Cavitation Within the Draft Tube of Pump-turbines. *J. Appl. Fluid. Mech.* **2025**, *18*, 2757–2774. [CrossRef]
16. Pang, S.; Zhu, B.; Shen, Y.; Chen, Z. Study on cavitating vortex rope characteristics of reversible pump-turbine under part load turbine condition. *Phys. Fluids* **2023**, *35*, 085131. [CrossRef]
17. Liu, G.; Sun, L.; Guo, P.; Li, Y.; Wang, W.; Wang, Z. Coherent structure analysis of double-helix vortex rope in pump turbine operating in turbine mode based on POD and DMD. *J. Energy Storage* **2025**, *128*, 117144. [CrossRef]
18. Mao, X.; Zheng, Y.; Qu, B.; Guo, C.; He, Z. Analysis on the internal flow field in vaneless space and draft tube of one reversible pump turbine during load rejection under turbine mode. In Proceedings of the IOP Conference Series: Earth and Environmental Science, Paris, France, 7–9 February 2018; IOP: London, UK, 2018; p. 012059.
19. Zhang, W.; Chen, Z.; Zhu, B.; Zhang, F. Pressure fluctuation and flow instability in S-shaped region of a reversible pump-turbine. *Renew. Energy* **2020**, *154*, 826–840. [CrossRef]
20. Li, Q.; Xin, L.; Xie, G.; Liu, S.; Wang, Q. Influence of guide vane profile change on draft tube flow characteristics of water pump turbine. *Processes* **2022**, *10*, 1494. [CrossRef]
21. Trivedi, C.; Cervantes, M.J. Fluid-structure interactions in Francis turbines: A perspective review. *Renew. Sustain. Energy Rev.* **2017**, *68*, 87–101. [CrossRef]
22. Wang, L.; Cui, J.; Shu, L.; Jiang, D.; Xiang, C.; Li, L.; Zhou, P. Research on the vortex rope control techniques in draft tube of Francis turbines. *Energies* **2022**, *15*, 9280. [CrossRef]
23. Anup, K.; Thapa, B.; Lee, Y.-H. Transient numerical analysis of rotor–stator interaction in a Francis turbine. *Renew. Energy* **2014**, *65*, 227–235. [CrossRef]
24. Xia, X.; Luo, H.; Li, S.; Wang, F.; Zhou, L.; Wang, Z. Characteristics and factors of mode families of axial turbine runner. *Int. J. Mech. Sci.* **2023**, *251*, 108356. [CrossRef]

25. Xu, B.; Chen, D.; Zhang, H.; Zhou, R. Dynamic analysis and modeling of a novel fractional-order hydro-turbine-generator unit. *Nonlinear Dyn.* **2015**, *81*, 1263–1274. [CrossRef]
26. Xu, B.; Luo, X.; Egusquiza, M.; Ye, W.; Liu, J.; Egusquiza, E.; Chen, D.; Guo, P. Nonlinear modal interaction analysis and vibration characteristics of a francis hydro-turbine generator unit. *Renew. Energy* **2021**, *168*, 854–864. [CrossRef]
27. Niu, L.; Sun, Q.; Ma, C.; Liao, J.; Pu, J. Research on Modal Analysis of Rotor Shaft System of Hydro-generator. In *Proceedings of the Journal of Physics: Conference Series, Taiwan, China, 21–23 May 2021*; IOP: London, UK, 2020; p. 042084.
28. Ma, Z.; Wu, Q. Study on Dynamic Characteristics of Rotor-bearing Model in the Hydraulic-mechanical-electric Coupled System of Hydro Generator Unit. In Proceedings of the 16th International Symposium on Transport Phenomena and Dynamics of Rotating Machinery, Honolulu, HI, USA, 10–15 April 2016.
29. Cao, J.; Luo, Y.; Shi, Y.; Liu, X.; Xu, D.; Wang, Y.; Zhai, L.; Wang, Z. A review of hydro-turbine unit rotor system dynamic behavior: Multi-field coupling of a three-dimensional model. *Phys. Fluids* **2024**, *36*, 121304. [CrossRef]
30. Krishnan, N.S.R.; Prasad, S.; Vaibhav, M.S.; Kumar, S. Numerical investigation of turbulence modeling schemes. In Proceedings of the 5th International Conference on Innovative Design, Analysis & Development Practices in Aerospace & Automotive Engineering: I-DAD'22, Chennai, India, 24 February 2022; AIP Publishing: Melville, NY, USA, 2023; p. 020016.
31. Menter, F.R. *Improved Two-Equation K-Omega Turbulence Models for Aerodynamic Flows*; NASA: Washington, DC, USA, 1992.
32. Hellsten, A. Some improvements in Menter's k-omega SST turbulence model. In Proceedings of the 29th AIAA, Fluid Dynamics Conference, Albuquerque, NM, USA, 15–18 June 1998; p. 2554.
33. Li, Y.; Chen, L.; Xu, J.; Yu, A. Research on the Flow Evolution and Runner Force Characteristics of a Pump-Turbine Under Cavitation Effects. *Appl. Sci.* **2026**, *16*, 2898. [CrossRef]

Disclaimer/Publisher's Note: The statements, opinions and data contained in all publications are solely those of the individual author(s) and contributor(s) and not of MDPI and/or the editor(s). MDPI and/or the editor(s) disclaim responsibility for any injury to people or property resulting from any ideas, methods, instructions or products referred to in the content.